METHODOLOGY OF WAVEFORM INVERSION FOR ACOUSTIC ORTHORHOMBIC MEDIA

HUI WANG* and ILYA TSVANKIN

Center for Wave Phenomena, Colorado School of Mines, Golden, CO 80401, U.S.A.
ilya@mines.edu
* Present address: CGG, 10300 Town Park Drive, Houston, TX 77072, U.S.A.

ABSTRACT

Wang, H. and Tsvankin, I., 2018. Methodology of waveform inversion for acoustic orthorhombic media. *Journal of Seismic Exploration*, 27: 201-226.

   Three-dimensional seismic waveform inversion (WI) for anisotropic media is highly challenging due to its computational cost and trade-offs between multiple model parameters. Here, we develop a methodology of 3D WI for orthorhombic media in the acoustic approximation using two mixed-domain modeling algorithms, one of which is based on low-rank decomposition and the other on the generalized pseudospectral method. Numerical testing shows that both techniques produce kinematically accurate compressional wavefields with an acceptable computational cost. To take advantage of the superior stability and accuracy of the low-rank-decomposition-based method, it is employed to simulate both the forward and adjoint wavefields. The gradient of the data-difference objective function, however, is more convenient to obtain from the wave equations derived with the pseudospectral method. The inversion is conducted with a limited-memory version of the quasi-Newton optimization algorithm. Under the assumption that the symmetry-plane orientation is known, we invert wide-azimuth data for all six parameters of acoustic orthorhombic media. The performance of the developed wavefield-extrapolation and gradient-computation algorithms is evaluated for a medium with Gaussian anomalies in each parameter. Then we apply the method to a modified SEG/EAGE overthrust model to demonstrate the feasibility of waveform inversion and illustrate parameter trade-offs for structurally complicated orthorhombic media.

KEY WORDS: waveform inversion, orthorhombic media, seismic anisotropy,
                      low-rank decomposition, pseudospectral method.

INTRODUCTION

Waveform inversion (WI) has been an active area of research since its formal introduction by Lailly (1983) and Tarantola (1984). However, most existing waveform-inversion techniques are designed to recover just P-wave velocity due to the high computational cost and the intrinsic nonlinearity of the inverse problem. Recently, WI has been extended to both acoustic and elastic transversely isotropic models with a vertical symmetry axis (VTI). Gholami et al. (2013) present a waveform-inversion case study for Valhall field using a 2D acoustic VTI algorithm. Kamath and Tsvankin (2013) apply elastic WI to multicomponent reflection data for layer-cake VTI models to obtain the interval medium parameters. Elastic WI for laterally heterogeneous VTI media is developed by Kamath and Tsvankin (2016), who apply their algorithm to transmission data for models with Gaussian anomalies in the Thomsen parameters. They also perform sensitivity analysis using the radiation patterns for elastic VTI media.

Transverse isotropy, however, cannot describe many subsurface formations that exhibit orthorhombic symmetry due to the influence of aligned fractures and nonhydrostatic stresses. Orthorhombic models have been successfully used in processing of wide-azimuth reflection and VSP data and fracture characterization (Tsvankin, 1997; Tsvankin and Grechka, 2011; Birdus et al., 2012; Thomas et al., 2012; Wang and Wilkinson, 2012; Karazincir and Orumwense, 2014; Mathewson et al., 2015).

In this paper, we focus on acoustic orthorhombic models described by a simplified wave equation that preserves P-wave kinematics (Alkhalifah, 1998, 2000). Whereas the acoustic approximation is generally adequate for diving (refracted) waves, it has well-known limitations in modeling reflection amplitudes, especially for long-offset data. Nonetheless, acoustic isotropic and VTI models are widely used in WI because they substantially reduce computational cost and are described by a smaller number of independent parameters. As shown by Tsvankin (1997, 2012), P-wave kinematic signatures in elastic orthorhombic media with a fixed orientation of the symmetry planes are controlled by six parameters – the P-wave vertical velocity V_{P0} and anisotropy coefficients $\varepsilon^{(1)}$, $\varepsilon^{(2)}$, $\delta^{(1)}$, $\delta^{(2)}$, and $\delta^{(3)}$ (assuming one of the symmetry planes to be horizontal). The same six parameters are fully responsible for P-wave propagation in acoustic orthorhombic media (Alkhalifah, 2000). Parameterization-related issues for tomography and waveform inversion in orthorhombic media are discussed in the acoustic approximation by Fowler (2015), Alkhalifah et al. (2016), and Masmoudi and Alkhalifah (2016).

Waveform inversion for complicated models such as orthorhombic has to be performed with efficient wavefield simulators. Two categories of methods have been proposed to model P-wave propagation in anisotropic

media: coupled systems and mixed-domain wavefield extrapolators. The coupled systems were originally introduced for TI media (Zhou et al., 2006a,b; Fletcher et al., 2008, 2009; Fowler et al., 2010; Duveneck and Bakker, 2011) and later extended to orthorhombic symmetry (Zhang and Zhang, 2011; Fowler and King, 2011). However, those systems produce shear-wave "artifacts" (Grechka et al., 2004) caused by setting the shear-wave velocity along the symmetry-axis direction to zero.

The mixed-domain wavefield extrapolators, on the other hand, can simulate pure P-wave propagation. In this paper, we implement two efficient mixed-domain wavefield extrapolators: those based on low-rank decomposition (Song and Alkhalifah, 2013; Fomel et al., 2013b) and generalized pseudospectral methods (Fowler and Lapilli, 2012). Low-rank-decomposition-based wavefield extrapolators are used for both forward and adjoint modeling. The inversion gradients, however, are more easily derived and computed using the wave equations from generalized pseudospectral methods. Hence, combining these two extrapolators for modeling and gradient calculation proves to be useful in implementing WI in acoustic orthorhombic media.

Most published algorithms for waveform inversion in orthorhombic media estimate a subset of the model parameters (Royle, 2011; Baydin et al., 2015; Albertin et al., 2016; Oh and Alkhalifah, 2016; Xie et al., 2017). Therefore, unless accurate a priori information about the model is available, inversion results can be strongly biased. It is preferable to perform simultaneous inversion for all pertinent model parameters. In this paper, we develop a WI methodology to simultaneously recover all six parameters of acoustic orthorhombic media.

We start by introducing P-wave simulators based on the low-rank matrix decomposition and generalized pseudospectral mixed-domain operators along with the corresponding numerical adjoint systems. The adjoint-state method is employed to derive the gradients of the data-difference objective function with respect to the six chosen parameters of orthorhombic media. Multiparameter waveform inversion is then carried out using a nonlinear optimization algorithm. Synthetic examples for orthorhombic models with realistic structural complexity illustrate gradient computation and waveform inversion of wide-azimuth surface data.

MIXED-DOMAIN WAVEFIELD SIMULATOR

The starting point for deriving pure-mode mixed-domain wavefield extrapolators is the dispersion relation of the corresponding wave mode. These extrapolators satisfy a general equation of the form (Du et al., 2014):

$$\partial_{tt} u(\mathbf{k}, t) + \mathbf{\Phi}(\mathbf{x}, \mathbf{k})\, u(\mathbf{k}, t) = 0\,, \tag{1}$$

where $u(\mathbf{k}, t)$ denotes the scalar wavefield variable in the time-wavenumber domain, $\mathbf{k}$ is the wave vector, ∂_{tt} is the second time-derivative operator, and $\mathbf{\Phi}(\mathbf{x}, \mathbf{k})$ is a linear operator defined in the mixed (spatial and wavenumber) domain; the source term in eq. (1) is ignored. In isotropic media, the mixed-domain operator $\mathbf{\Phi}$ reduces to

$$\mathbf{\Phi}(\mathbf{x}, \mathbf{k}) = v^2(\mathbf{x})\, |\mathbf{k}|^2\,, \tag{2}$$

where $v(\mathbf{x})$ is the velocity. If the model is anisotropic, the mixed-domain operator for a selected mode can be obtained from the corresponding dispersion relation using the Christoffel equation.

P-wave velocity in orthorhombic media can be described by six Thomsen-style parameters (Tsvankin, 1997, 2012): the P-wave vertical velocity V_{P0} and the anisotropy coefficients $\varepsilon^{(1)}$, $\varepsilon^{(2)}$, $\delta^{(1)}$, $\delta^{(2)}$, and $\delta^{(3)}$ (the Cartesian coordinate planes are assumed to coincide with the planes of symmetry). Expressions for these parameters in terms of the stiffnesses are given in the Appendix. An important advantage of Tsvankin's notation is that it reduces the number of independent parameters responsible for P-wave kinematics from nine to six. The same six parameters control the wave equation in acoustic orthorhombic media (Alkhalifah, 2000).

Throughout the paper we consider one of the symmetry planes to be horizontal, but the wavefield propagators discussed here can handle orthorhombic models with arbitrary symmetry-plane orientation. Our inversion algorithm operates with the velocities V_{Pz}, V_{Py}, V_{Px}, $V_{\mathrm{nmo}}^{(1)}$, $V_{\mathrm{nmo}}^{(2)}$, and $V_{\mathrm{nmo}}^{(3)}$ defined in the Appendix. The parameters $V_{\mathrm{Pz}} = V_{\mathrm{P0}}$, V_{Px}, and V_{Py} are the P-wave velocities in the coordinate directions. The normal-moveout (NMO) velocities $V_{\mathrm{nmo}}^{(1)}$ and $V_{\mathrm{nmo}}^{(2)}$ are those measured in the x_2- and x_1-directions, respectively, above a horizontal orthorhombic layer. The NMO velocity $V_{\mathrm{nmo}}^{(3)}$ is defined by Fowler and Lapilli (2012) in a similar fashion for the horizontal plane.

The Christoffel matrix in acoustic orthorhombic media can be symbolically written as:

$$\mathbf{G} = \mathbf{K}\,\mathbf{M}\,\mathbf{K}^{\mathsf{T}}\,, \tag{3}$$

where the matrices $\mathbf{K}$ and $\mathbf{K}^{\mathsf{T}}$ contain wavenumbers, and $\mathbf{M}$ depends only

on the medium parameters. The specific forms of **K** and **M** are shown in the Appendix [eqs. (A-9) and (A-10)].

The P-wave dispersion relation is then obtained by solving the characteristic equation of the eigenvalue-eigenvector problem:

$$\det\left(\mathbf{G} - \omega^2\,\mathbf{I}\right) = 0\,,\tag{4}$$

which results in a cubic equation in ω^2 given in the Appendix [eq. (A-11)]. Note that the P-wave dispersion relation corresponds to the largest root of the cubic equation, which can be solved analytically. Then the mixed-domain operator is obtained as

$$\mathbf{\Phi}(\mathbf{x}, \mathbf{k}) = \omega^2\,.\tag{5}$$

The next step is to find a numeric solution of eq. (1) for the generic-form mixed-domain wavefield extrapolator. Note that for a spatially invariant operator $\Phi(\mathbf{x},\ \mathbf{k}) = \Phi(\mathbf{k})$, eq. (1) reduces to a system of ordinary differential equations with the time variable t, which has the formal solution

$$u(\mathbf{k}, t \pm \Delta t) = e^{\pm i\sqrt{\Phi(\mathbf{k})}\,\Delta t}\,u(\mathbf{k}, t)\,.\tag{6}$$

Eq. (6) has been extensively discussed in the literature (Tal-Ezer, 1986; Tal-Ezer et al., 1987; Etgen and Dellinger, 1989; Zhang and Zhang, 2009; Du et al., 2014). Adding the outgoing and incoming solutions of eq.(6), one arrives at the time-stepping formula:

$$u(\mathbf{k}, t + \Delta t) + u(\mathbf{k}, t - \Delta t) = 2\cos\left(\sqrt{\Phi(\mathbf{k})}\,\Delta t\right)u(\mathbf{k}, t)\,.\tag{7}$$

Applying the Fourier transform to both sides of eq. (7), we obtain the space-domain wavefields:

$$u(\mathbf{x}, t + \Delta t) + u(\mathbf{x}, t - \Delta t) = \mathcal{F}^{-1}\left[2\cos\left(\sqrt{\Phi}\,\Delta t\right)\mathcal{F}\left[u(\mathbf{x}, t)\right]\right]\,,\tag{8}$$

where $\mathcal{F}[\cdot]$ and $\mathcal{F}^{-1}[\cdot]$ denote the forward and inverse Fourier transforms, respectively. If the mixed- domain operator $\mathbf{\Phi}(\mathbf{x},\ \mathbf{k})$ varies in space, the time-stepping formula (8) provides only an approximate solution to eq. (1). Solving eq. (8) is time-consuming because the number of inverse FFT's is equal to the number of the spatial grid points. We use two techniques described below to speed up this computation: low-rank decomposition (Fomel et al., 2013b) and the generalized pseudospectral method (Fowler and Lapilli, 2012).

Wavefield simulator based on low-rank decomposition

The low-rank-decomposition-based extrapolation algorithm used here follows the work by Fomel et al. (2013b). According to their approach, the first step is to discretize the cosine term of eq. (8) into a matrix:

$$\cos\left(\sqrt{\mathbf{\Phi}}\,\Delta t\right) = \frac{1}{2} \begin{bmatrix} \cos\left(\sqrt{\mathbf{\Phi}(\mathbf{x_1},\mathbf{k_1})}\,\Delta t\right) & \cdots & \cos\left(\sqrt{\mathbf{\Phi}(\mathbf{x_1},\mathbf{k_N})}\,\Delta t\right) \\ \vdots & \ddots & \vdots \\ \cos\left(\sqrt{\mathbf{\Phi}(\mathbf{x_M},\mathbf{k_1})}\,\Delta t\right) & \cdots & \cos\left(\sqrt{\mathbf{\Phi}(\mathbf{x_M},\mathbf{k_N})}\,\Delta t\right) \end{bmatrix}.$$
(9)

This matrix, called a "propagator", is iteratively applied to the wavefield during wave extrapolation. If the time step Δt is sufficiently small, eq. (9) has a low-rank feature, which means that the discretized matrix and its Hermitian have a large null space. This sparsity makes it possible to represent the matrix using a relatively small number of column and row vectors. Although singular value decomposition (SVD) is a common choice to select those vectors, it is impractical computationally because the dimension of the matrix in eq. (9) for 3D problems is extremely large (typically the number of rows and columns is on the order of 10^9).

A cheaper way to obtain those vectors is based on a randomized algorithm, which performs sparse matrix decomposition by selecting certain columns and rows of the original matrix. Symbolically, this decomposition takes the form of

$$\cos\left(\sqrt{\mathbf{\Phi}}\,\Delta t\right) \equiv \mathbf{W} = \mathbf{U}\,\mathbf{\Lambda}\,\mathbf{V},$$
(10)

where $\mathbf{W}$ is the $M \times N$ propagator matrix, $\mathbf{U}$ is the $M \times m$ matrix of selected columns, $\mathbf{V}$ is the $n \times N$ matrix of selected rows, $\mathbf{\Lambda}$ is a $m \times n$ full matrix of a relatively small size, where m and n are called the approximate numeric row and column ranks of the matrix $\mathbf{W}$ ($m \ll M$ and $n \ll N$). The obvious differences between this decomposition and SVD are that the columns of $\mathbf{U}$ are a subset of the columns of $\mathbf{W}$ rather than the eigenvectors of $\mathbf{W}\mathbf{W}^t$, the rows of $\mathbf{V}$ are a subset of the rows of $\mathbf{W}$ rather than the eigenvectors of $\mathbf{W}^t\mathbf{W}$, and $\mathbf{\Lambda}$ is a small full matrix rather than a diagonal matrix consisting of the eigenvalues obtained by SVD.

In a typical implementation, one multiplies the matrices $\mathbf{U}$ and $\mathbf{\Lambda}$:

$$\mathbf{L} \equiv \mathbf{U}\,\mathbf{\Lambda},$$
(11)

which yields the following low-rank decomposition:

$$\cos\left(\sqrt{\mathbf{\Phi}}\Delta t\right) \equiv \mathbf{W} = \mathbf{L}\,\mathbf{R}\,, \tag{12}$$

where $\mathbf{R}$ coincides with $\mathbf{V}$ [eq. (10)]. Using eq. (12), one can iteratively propagate the wavefield along the time axis:

$$u(\mathbf{x}, t + \Delta t) + u(\mathbf{x}, t - \Delta t) = 2\,\mathbf{L}\,\mathcal{F}^{-1}\Big[\mathbf{R}\,\mathcal{F}\left[u(\mathbf{x}, t)\right]\Big]\,, \tag{13}$$

where $\mathbf{R}$ and $\mathbf{L}$ are applied in the wavenumber and spatial domains, respectively.

Generalized pseudospectral wavefield simulator

Low-rank decomposition methods can accurately simulate wave propagation because they do not involve any approximations of the corresponding dispersion relations. However, the matrix decomposition is purely numeric and the decomposed matrices cannot be expressed explicitly in terms of the medium parameters. This causes a problem for adjoint-state techniques, where the wave equation needs to be differentiated with respect to the medium parameters.

The pseudospectral method (Kosloff and Baysal, 1982) provides an efficient way to simulate wavefields while maintaining an explicit form of the wave equation. Its extension to orthorhombic media was presented by Fowler and Lapilli (2012), who proposed the generalized pseudospectral method. That method approximates the wavefield derivatives using global basis functions, rather than local finite-differences. First, the cosine term in eq. (8) is expanded in a two-term Taylor series

$$\cos\left(\sqrt{\mathbf{\Phi}}\,\Delta t\right) \approx 1 - \frac{1}{2}(\Delta t)^2\,\mathbf{\Phi}\,. \tag{14}$$

The time-stepping formula (8) then becomes:

$$u(\mathbf{x}, t + \Delta t) + u(\mathbf{x}, t - \Delta t) = 2u(\mathbf{x}, t) - (\Delta t)^2 \mathcal{F}^{-1}\Big[\mathbf{\Phi}\mathcal{F}\left[u(\mathbf{x}, t)\right]\Big]\,. \tag{15}$$

Because the mixed-domain operator $\mathbf{\Phi}(\mathbf{x}, \mathbf{k})$ involves a certain form of spatial derivatives, eq. (15) implements the generalized pseudospectral method with Fourier basis functions. However, application of eq. (15) is still

hampered by the fact that the operator $\mathbf{\Phi}(\mathbf{x}, \mathbf{k})$ varies spatially and appears inside the inverse Fourier transform. To use Fast Fourier transforms, the mixed-domain operator must be represented in separable form:

$$\mathbf{\Phi}(\mathbf{x}, \mathbf{k}) = \sum_{i=1}^{N} f_i(\mathbf{x})\, g_i(\mathbf{k}),$$

$$(16)$$

where N is the number of separable terms, and $f_i(\mathbf{x})$ and $g_i(\mathbf{k})$ are the pure spatial- and wavenumber-domain operators, respectively.

For an acoustic orthorhombic medium with the symmetry planes that coincide with the Cartesian coordinate planes, the separable mixed-domain operator takes the form [eq. (13) in Fowler and Lapilli (2012)]:

$$\mathbf{\Phi}(\mathbf{x}, \mathbf{k}) \approx V_{\mathrm{Px}}^2 k_x^2 + V_{\mathrm{Py}}^2 k_y^2 + V_{\mathrm{Pz}}^2 k_z^2 - \frac{V_{\mathrm{Px}}^2\,(V_{\mathrm{Py}}^2 - (V_{\mathrm{nmo}}^{(3)})^2)}{V_{\mathrm{r}}^2}\,\frac{k_x^2\,k_y^2}{k^2}$$

$$- \frac{V_{\mathrm{Pz}}^2\,(V_{\mathrm{Px}}^2 - (V_{\mathrm{nmo}}^{(2)})^2)}{V_{\mathrm{r}}^2}\,\frac{k_x^2\,k_z^2}{k^2} - \frac{V_{\mathrm{Pz}}^2\,(V_{\mathrm{Py}}^2 - (V_{\mathrm{nmo}}^{(1)})^2)}{V_{\mathrm{r}}^2}\,\frac{k_y^2\,k_z^2}{k^2},$$

$$(17)$$

where V_{r} is a certain reference velocity, and the other velocities are defined in the Appendix.

Once the mixed-domain operator is separated into the pure spatial- and wavenumber-domain operators [eq. (17)], the corresponding time-stepping formula can be expressed as (Fowler and Lapilli, 2012):

$$u(\mathbf{x}, t + \Delta t) + u(\mathbf{x}, t - \Delta t) = 2u(\mathbf{x}, t) - (\Delta t)^2 \sum_i f_i(\mathbf{x}) \mathcal{F}^{-1}\Big[g_i(\mathbf{k})\mathcal{F}\big[u(\mathbf{x}, t)\big]\Big].$$

$$(18)$$

Comparison of two extrapolators

Although both low-rank-decomposition-based and generalized pseudo-spectral methods can synthesize kinematically correct P-wavefields, the simulated amplitudes differ from those in elastic media. Such amplitude distortions are inevitable in the acoustic approximation. However, generalized pseudospectral methods introduce additional approximations to the P-wave dispersion relation to achieve a separable form of the mixed-domain operators. This approximation may cause problems during the inversion because model updates do not necessarily satisfy the assumptions of the method. In such cases, the wavefield simulation becomes either unstable or

inaccurate. Therefore, we employ low-rank decomposition to model both the forward and adjoint wavefields.

In terms of efficiency, the low-rank decomposition and generalized pseudospectral methods are similar. For each time step, time complexity of both algorithms is linear-logarithmic in the number of the spatial grid points because both techniques are FFT-based. Prior to the wave extrapolation stage, low-rank decomposition has additional linear time-complexity in the number of spatial grid points (Fomel et al., 2013b), but it can be ignored compared to the time-stepping part of the algorithm. Pestana and Stoffa (2010) and Fomel et al. (2013b) show that low-rank decomposition-based extrapolators are typically less expensive than their pseudospectral counterparts because they require fewer applications of FFT in the time stepping.

Absorbing boundary condition

An important component of the numerical simulation is boundary conditions. For low-rank-based and generalized pseudospectral simulators, the absorbing boundary condition can be implemented by adding an exponentially decaying term to the wavefield after applying the propagators:

$$u(\mathbf{k}, t \pm \Delta t) = e^{\mp \alpha(\mathbf{x})} e^{\pm i \sqrt{\mathbf{\Phi(k)}} \, \Delta t} \, u(\mathbf{k}, t) \,, \tag{19}$$

where $\alpha(\mathbf{x})$ is the damping profile with nonzero values at the boundary. Adding the outgoing and incoming solutions yields the two-step time extrapolation formula in the spatial domain:

$$u(\mathbf{x}, t + \Delta t) + e^{-2\alpha(\mathbf{x})} \, u(\mathbf{x}, t - \Delta t) = e^{-\alpha(\mathbf{x})} \mathcal{F}^{-1} \left[2 \cos\left(\sqrt{\mathbf{\Phi}} \Delta t \right) \mathcal{F} \left[u(\mathbf{x}, t) \right] \right] . \tag{20}$$

Employing the approach discussed in the previous two sections, one can arrive at the following two-step formula for low-rank decomposition extrapolators:

$$u(\mathbf{x}, t + \Delta t) + e^{-2\alpha(\mathbf{x})} \, u(\mathbf{x}, t - \Delta t) = 2 e^{-\alpha(\mathbf{x})} \mathbf{L} \, \mathcal{F}^{-1} \left[\mathbf{R} \, \mathcal{F} \left[u(\mathbf{x}, t) \right] \right] . \tag{21}$$

For generalized pseudospectral extrapolators, the corresponding equation is:

$$u(\mathbf{x}, t + \Delta t) + e^{-2\alpha(\mathbf{x})} u(\mathbf{x}, t - \Delta t)$$

$$= e^{-\alpha(\mathbf{x})} \left\{ 2u(\mathbf{x}, t) - (\Delta t)^2 \sum_i f_i(\mathbf{x}) \mathcal{F}^{-1} \Big[g_i(\mathbf{k}) \mathcal{F}\big[u(\mathbf{x}, t)\big] \Big] \right\}. \tag{22}$$

Adjoint wavefield propagation

Seismic waveform inversion is often performed using adjoint methods because the cost of computing the Fréchet derivatives of the objective function is prohibitively high (Fichtner, 2010). Such methods operate with so-called adjoint wavefield variables, which satisfy the adjoint wave equations. If the wave equations used in the forward simulations are self-adjoint, the corresponding equations retain the same form. On the other hand, if the wave equations for forward simulation are not self-adjoint, such as the ones we use in this paper (based on low-rank decomposition and generalized pseudospectral methods), the adjoint wave equations have a different form and need to be solved separately.

Because the forward wavefield simulators are basically successive matrix-vector multiplications applied to wavefield vectors, the numerical adjoint wavefield simulators represent the transposed matrices successively operating with those wavefield vectors. The mixed-domain adjoint wave equations can be written in the following generic form similar to eq. (1):

$$\partial_{tt} u(\mathbf{k}, t) + \tilde{\mathbf{\Phi}}(\mathbf{x}, \mathbf{k})\, u(\mathbf{k}, t) = 0\,, \tag{23}$$

where $\tilde{\mathbf{\Phi}}(\mathbf{x}, \mathbf{k})$ is the numeric adjoint mixed-domain operator. In the case of the low-rank decomposition simulator, the adjoint mixed-domain operator is:

$$\tilde{\mathbf{\Phi}}(\mathbf{x}, \mathbf{k}) = \mathbf{R}^\mathsf{T} \mathbf{L}^\mathsf{T}\,, \tag{24}$$

where " T " indicates the matrix transpose, and $\mathbf{L}$ and $\mathbf{R}$ are defined in eqs. (11) and (12). The corresponding time-stepping formula then becomes:

$$u(\mathbf{x}, t + \Delta t) + u(\mathbf{x}, t - \Delta t) = \mathcal{F}^{-1} \Big[\mathbf{R}^\mathsf{T} \mathcal{F} \big[\mathbf{L}^\mathsf{T} u(\mathbf{x}, t) \big] \Big]\,, \tag{25}$$

which is different from the forward time-stepping eq. (13).

WAVEFORM INVERSION

In addition to seismic wavefield simulators, waveform inversion requires well-designed objective functions and efficient large-scale nonlinear optimization algorithms, which are discussed below.

Objective function

Waveform inversion is performed by minimizing a certain objective function, most often the l_2-norm data difference. Due to the high nonlinearity of the problem, minimization is often carried out by gradually increasing the frequency bandwidth starting with low frequencies. Such cascaded inversions typically assume the existence of ultra low-frequency data, which are often missing in seismic acquisition. The reliance on low frequencies can be mitigated, for example, by employing envelope-based objective functions (Wu et al., 2014; Luo and Wu, 2015).

Here, we consider only the classical l_2-norm data difference, which is defined as

$$\mathcal{J}_{\text{dat}} = \frac{1}{2} \sum_{i \in \Gamma_x} \left\| \mathbf{d}_i^{\text{cal}} - \mathbf{d}_i^{\text{obs}} \right\|^2 , \tag{26}$$

where the subscript i denotes the data coordinate, Γ_x is an index set for the data coordinates, and $\mathbf{d}_i^{\text{cal}}$ and $\mathbf{d}_i^{\text{obs}}$ are the calculated and observed discrete-time data (respectively) for a given source-receiver pair that belongs to the N_t - dimensional vector space $\mathbb{R}^{N_t}$, where N_t is the number of time steps in numerical simulations. The data are obtained by applying a binning operator $\mathbf{W}$ to the wavefield:

$$\mathbf{d}_i = \sum_j W_{ij} \, \mathbf{u}_j . \tag{27}$$

For the ℓ_2-norm data difference in eq. (26), the adjoint source function used for modeling the adjoint variables is

$$\mathbf{f}^a = \mathbf{d}^{\text{cal}} - \mathbf{d}^{\text{obs}} . \tag{28}$$

Waveform-inversion gradients

To compute the gradients of the objective function using the adjoint-state method (Tarantola, 1988; Tromp et al., 2005; Plessix, 2006; Fichtner et al., 2006a,b; Liu and Tromp, 2008; Chen, 2011), one can augment the objective function:

$$\chi = \mathcal{J} - \langle \lambda, F \rangle \,, \tag{29}$$

where the symbol $<\cdot, \cdot>$ denotes the inner product in the L_2-space (to which the state and adjoint variables belong), and F is the discretized state equation:

$$F = \partial_{tt}\, u(\mathbf{k}, t) + \boldsymbol{\Phi}(\mathbf{x}, \mathbf{k})\, u(\mathbf{k}, t) - f^s = 0 \,, \tag{30}$$

where f^s is the source term. The adjoint variable λ satisfies the discretized adjoint equation:

$$F^{\mathsf{T}} = \partial_{tt}\, \lambda(\mathbf{k}, t) + \tilde{\boldsymbol{\Phi}}(\mathbf{x}, \mathbf{k})\lambda(\mathbf{k}, t) - f^a = 0 \,, \tag{31}$$

where f^a is the adjoint source term. The gradients of the original objective function are then derived by setting the derivatives of the function χ [eq. (29)] with respect to the medium parameters to zero:

$$\frac{\partial \chi}{\partial m} = \frac{\partial \mathcal{J}}{\partial m} - \left\langle \lambda, \frac{\partial F}{\partial m} \right\rangle = 0 \,. \tag{32}$$

The low-rank decomposition simulator for acoustic orthorhombic media does not yield a closed-form wave equation. Therefore, we elect to use the wave equation produced with the generalized pseudospectral method to compute the term $\partial F/\partial m$ in eq. (32), which is required to obtain the gradients. Deriving the separable mixed-domain operator [eq. (17)] from the generalized pseudospectral method, and substituting the parameters V_{Px}^2, V_{Py}^2, V_{Pz}^2, V_{nmo1}^2, V_{nmo2}^2, and V_{nmo3}^2 for m yields

$$\frac{\partial \mathcal{J}}{\partial (V_{\mathrm{Px}}^2)} = \left\langle \lambda, \left(k_x^2 - \frac{V_{\mathrm{Py}}^2 - V_{\mathrm{nmo3}}^2}{V_{\mathrm{r}}^2} \frac{k_x^2\, k_y^2}{k^2} - \frac{V_{\mathrm{Pz}}^2}{V_{\mathrm{r}}^2} \frac{k_x^2\, k_z^2}{k^2} \right) u \right\rangle \,, \tag{33}$$

$$\frac{\partial \mathcal{J}}{\partial \left(V_{\text{Py}}^2\right)} = \left\langle \lambda, \left(k_y^2 - \frac{V_{\text{Px}}^2}{V_{\text{r}}^2} \frac{k_x^2 k_y^2}{k^2} - \frac{V_{\text{Pz}}^2}{V_{\text{r}}^2} \frac{k_y^2 k_z^2}{k^2}\right) u \right\rangle,$$

(34)

$$\frac{\partial \mathcal{J}}{\partial (V_{\text{Pz}}^2)} = \left\langle \lambda, \left(k_z^2 - \frac{V_{\text{Px}}^2 - V_{\text{nmo2}}^2}{V_{\text{r}}^2} \frac{k_x^2 k_z^2}{k^2} - \frac{V_{\text{Py}}^2 - V_{\text{nmo1}}^2}{V_{\text{r}}^2} \frac{k_y^2 k_z^2}{k^2}\right) u \right\rangle,$$

(35)

$$\frac{\partial \mathcal{J}}{\partial (V_{\text{nmo1}}^2)} = \left\langle \lambda, \left(\frac{V_{\text{Pz}}^2}{V_{\text{r}}^2} \frac{k_y^2 k_z^2}{k^2}\right) u \right\rangle,$$

(36)

$$\frac{\partial \mathcal{J}}{\partial (V_{\text{nmo2}}^2)} = \left\langle \lambda, \left(\frac{V_{\text{Pz}}^2}{V_{\text{r}}^2} \frac{k_x^2 k_z^2}{k^2}\right) u \right\rangle,$$

(37)

$$\frac{\partial \mathcal{J}}{\partial (V_{\text{nmo3}}^2)} = \left\langle \lambda, \left(\frac{V_{\text{Px}}^2}{V_{\text{r}}^2} \frac{k_x^2 k_y^2}{k^2}\right) u \right\rangle,$$

(38)

where u and λ are the wavefield variables found from the state eq. (30) and the adjoint eq. (31), respectively.

SYNTHETIC EXAMPLES

Gradient computation

First, we test the computation of the inversion gradient on a relatively simple orthorhombic model with a Gaussian anomaly in each parameter (Fig.1). As illustrated in Fig. 2a, the anomalies for different parameter fields do not overlap. The wavefield is excited by an areal source array located at the surface (Fig. 2b). To remove the influence of illumination on the inversion results, we put receivers at each grid point on all six faces of the model cube.

Because the gradients govern the spatial positions and relative magnitudes of model updates, they help evaluate the performance of the chosen parameterization. Ideally, the gradient for each parameter should be nonzero only in the area of its Gaussian anomaly, which would imply the absence of trade-offs.
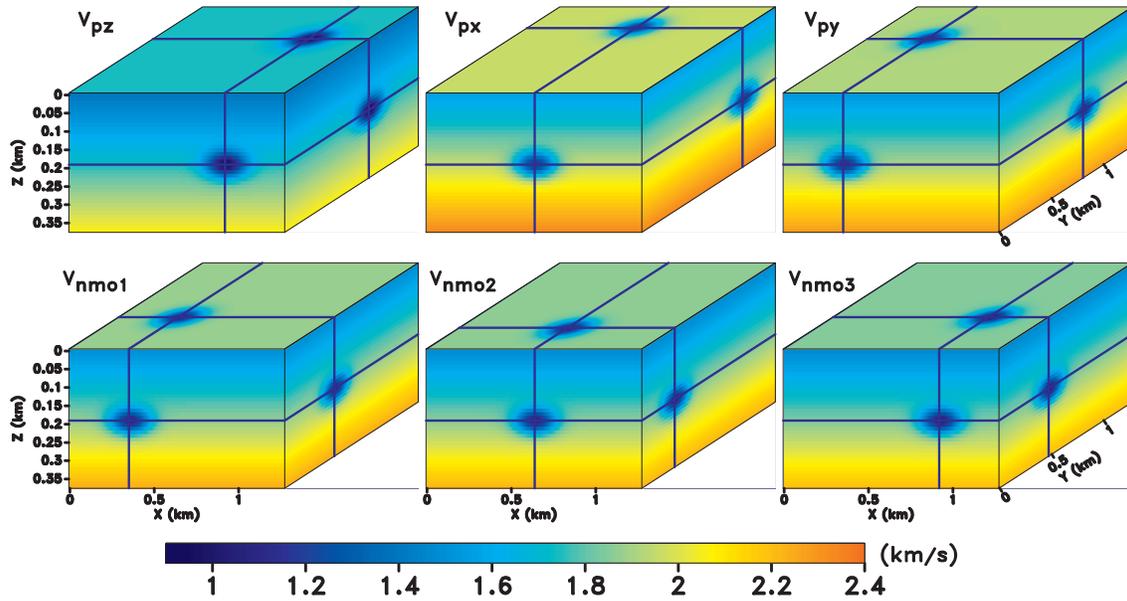
Fig. 1. 3D models of the six parameters of an acoustic orthorhombic medium. Gaussian anomalies are embedded in a background medium with linearly increasing velocities.
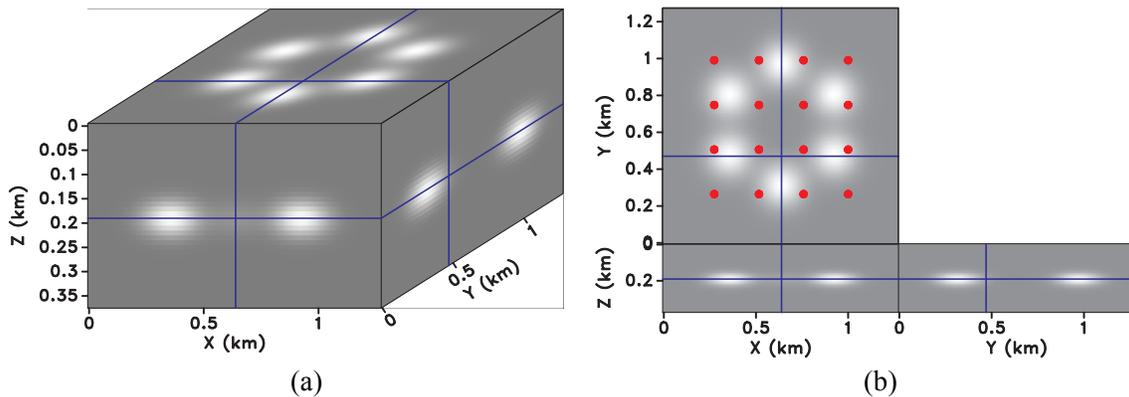

(a)

(b)

Fig. 2. (a) Six Gaussian anomalies from Fig. 1 plotted together. (b) The projections of the anomalies from Fig. 2a and the array of sources (red dots) at the surface.

Because the gradients govern the spatial positions and relative magnitudes of model updates, they help evaluate the performance of the chosen parameterization. Ideally, the gradient for each parameter should be nonzero only in the area of its Gaussian anomaly, which would imply the absence of trade-offs.

The gradients generally concentrate near the Gaussian anomalies but they are somewhat smeared in space, especially those for the parameters V_{nmo1}, V_{nmo2}, and V_{nmo3} (Fig. 3). Therefore, it is difficult to identify the precise locations of the anomalies for the three NMO velocities, which is an
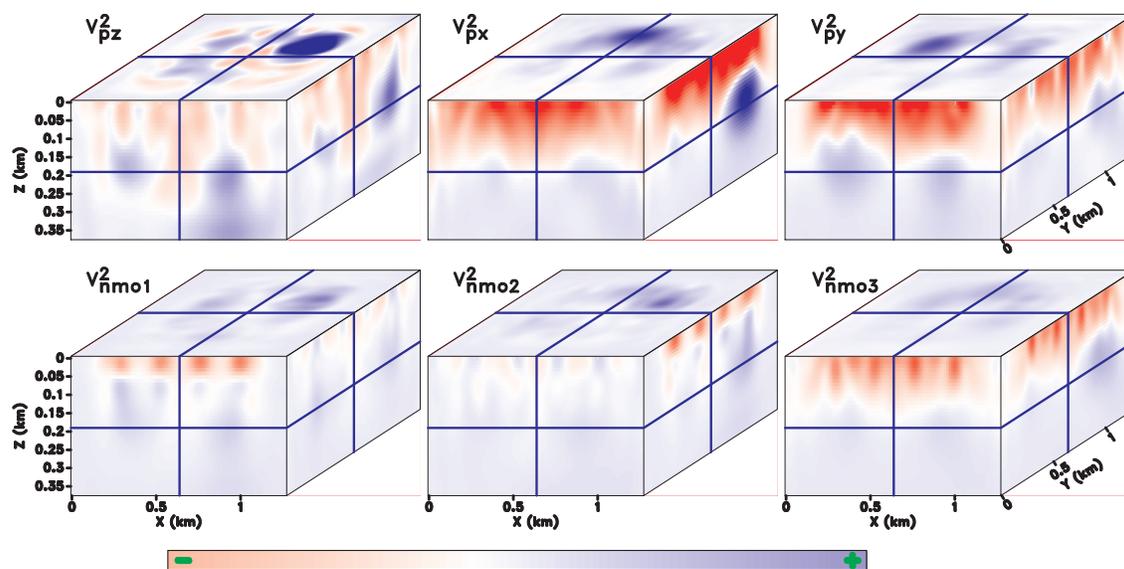
Fig. 3. WI gradients for the model from Fig. 1 computed with the ℓ_2-norm data difference. The gradients correspond to the background model with the linearly increasing velocities (Fig. 1). Notice that we just mark the positive and negative signs in the color bar. WI gradients represent only the descent directions during the iterative inversion process and their actual magnitudes are determined by the step length computed from line-searching algorithms.
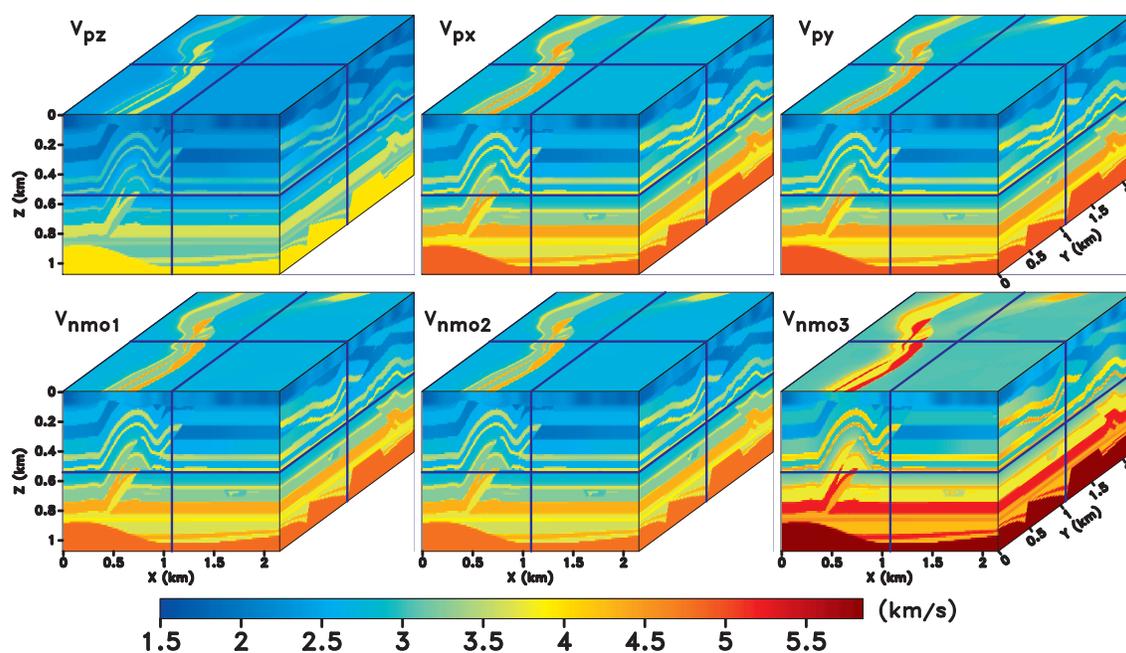

Fig. 4. Orthorhombic medium obtained from the SEG/EAGE overthrust model. The velocities are scaled from the original P-wave isotropic velocity field. The planes of symmetry coincide with the coordinate planes.

indication of coupling or trade-offs between the medium parameters. In contrast, the gradients for the coordinate-direction velocities V_{Pz}, V_{Px}, and V_{Py} show better-defined Gaussian-shape patterns near the anomalies, which indicates that they are more tightly constrained than the NMO velocities.

Inversion for the modified SEG/EAGE overthrust model

Next, we apply WI to synthetic data using an iterative gradient-based algorithm. Model updating is performed using a limited-memory variable metric method with box bounds (Benson and Moré, 2001; Thiébaut, 2002), which represents a version of the BFGS method (Liu and Nocedal, 1989; Nocedal, 1992; Kolda et al., 1998; Nocedal and Wright, 2009).

For this test, we use a modified portion of the SEG/EAGE overthrust model (Aminzadeh et al., 1997) overlaid by a water layer (Fig. 5). For simplicity, the symmetry-plane orientation is fixed throughout the model (one of the symmetry planes is horizontal), but the algorithm can potentially handle tilted orthorhombic media as well. To avoid the "inverse crime" of using the same wavefield simulators for modeling and inversion, the observed data (25 shot gathers) are produced with the generalized pseudospectral method, whereas low-rank decomposition is used for computing the forward and adjoint wavefields during model updating.
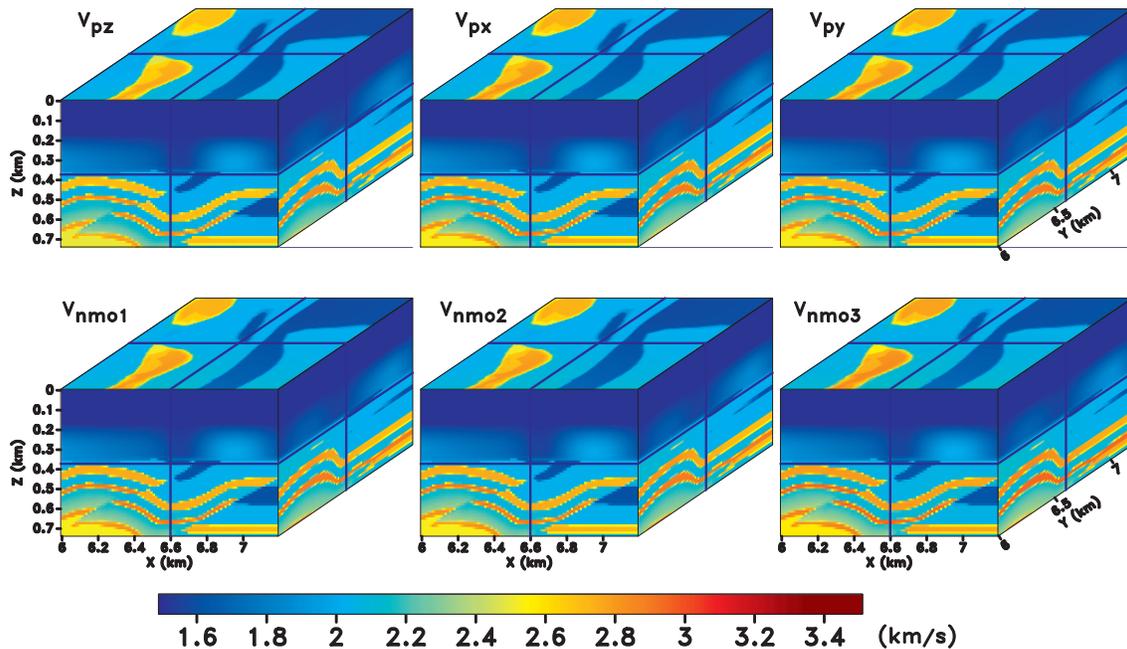

Fig. 5. Portion of the orthorhombic model from Fig. 4 with a water layer on top.

The shots are evenly spaced at the surface with a checkerboard pattern; the receivers are also located at the surface. We assume that the source function, which has an effective spectral band from 5 Hz to 55 Hz with a peak frequency around 20 Hz, is known.

The initial models for WI are obtained by strong smoothing of the actual velocity fields (Fig. 6). The WI is performed using the multiscale approach with five frequency bands: $0-8$ Hz, $0-16$ Hz, $0-32$ Hz, and $0-64$ Hz. We put masks around source positions to avoid large spurious updates in those areas, which is a typical practice in WI. The iterations for each frequency band are terminated when the objective function flattens out; the total number of iterations reached 102 with over 600 gradient evaluations. The inverted models (Fig. 7) show significant improvement over the initial ones, with important geologic structures such as faults, synclines, anticlines and low-velocity zones being better resolved.

For this particular acquisition geometry, the velocities V_{Pz}, V_{Py}, and V_{Py} are better constrained than the NMO velocities, which confirms the results of the gradient computation for the model with the Gaussian anomalies (Fig. 3). Due to the periodic nature of the FFT, spurious near-field artifacts are still present around source locations. These artifacts are more noticeable in the inverted NMO velocities, especially around the location ($z = 0.2$ km, $x = 0.4$ km, $y = 0.5$ km) in the V_{nmo2}-field.
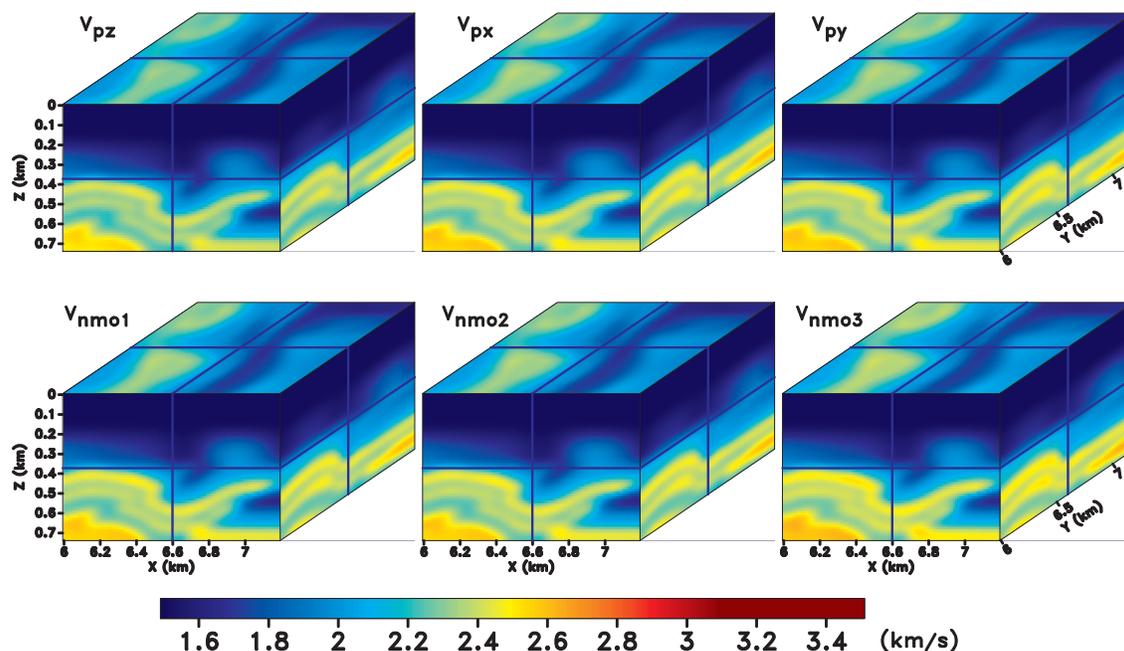

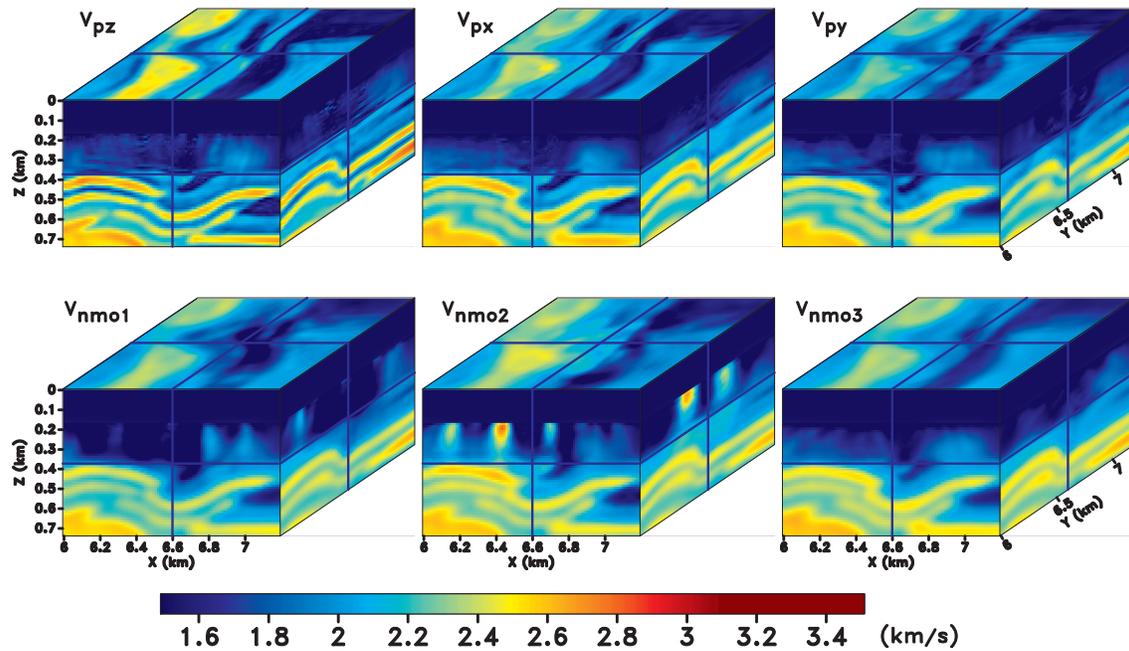Fig. 6. Initial parameter fields used to perform WI for the model in Fig. 5.

Fig. 7. Final inverted parameter fields.

To examine the inversion results in more detail, we plot the vertical profiles of the velocity V_{Pz} from the actual, initial, and inverted models (Fig.8a). Although not completely recovered, the inverted velocities are much closer to the actual values compared to the initial models.

Overall, this synthetic example demonstrates the potential of high-resolution parameter estimation for orthorhombic media using WI. The data fit is not perfect because of parameter trade-offs that produce a complicated, multimodal objective function. Nevertheless, the WI algorithm significantly reduces the data misfit and improves the accuracy of all model parameters. A more in-depth exploration of inversion strategies and parameter trade-offs is the subject of ongoing research.
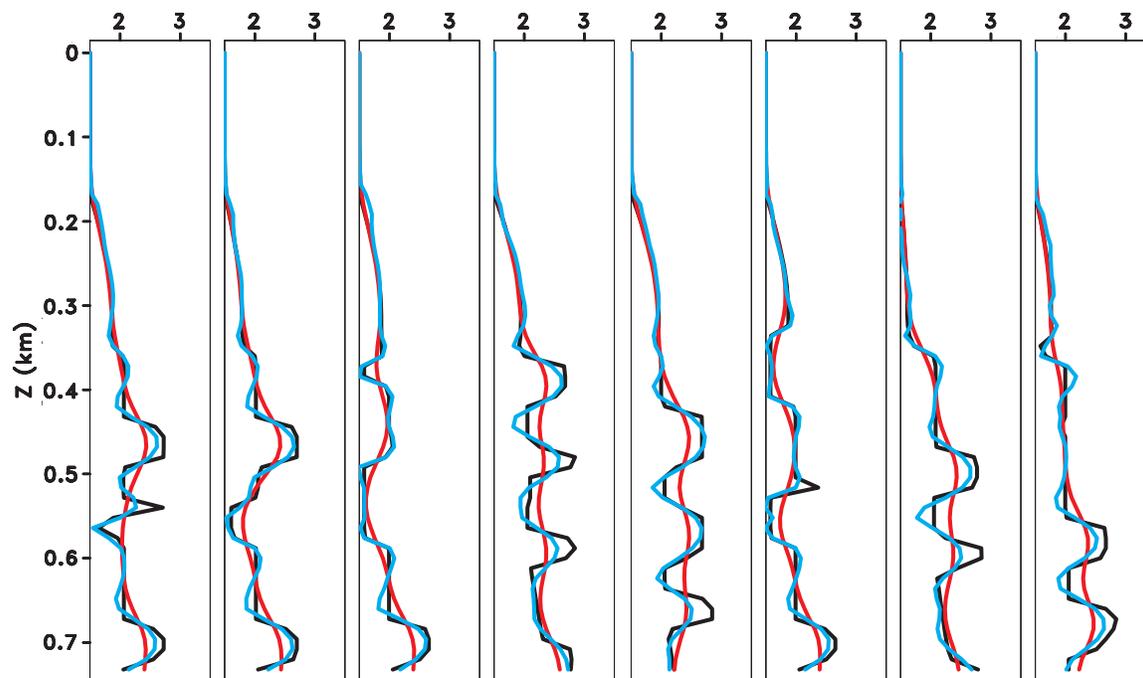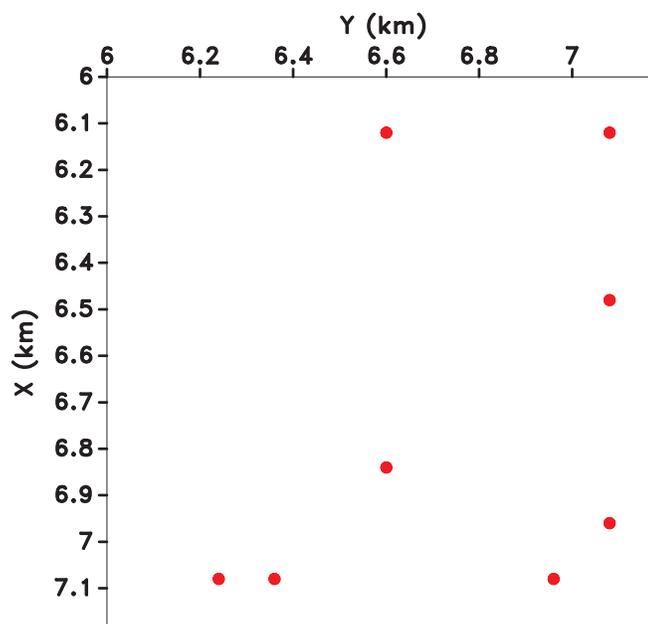
Fig. 8. (a) Vertical profiles of the actual (black), initial (red), and inverted (blue) velocity V_{Pz} (in km/s). (b) The locations of the velocity profiles. The profiles on plot (a) are arranged from left to right according to their locations [plot (b)] in the ascending order first in x and then in y.

CONCLUSIONS

We developed algorithms for 3D P-wave modeling and waveform inversion in acoustic orthorhombic media, and employed them to study the feasibility of parameter estimation from wide-azimuth surface data. Wavefield simulations are carried out with a mixed-domain extrapolator using low-rank decomposition. The gradient computation, however, is based on the wave equation obtained by the generalized pseudospectral method. The choice of wavefield extrapolator is explained by the superior accuracy and stability of the method based on low-rank decomposition.

The limited-memory variable metric method, used for model updating, performs reasonably well in terms of the convergence rate and computational cost. Our algorithm carries out multiparameter inversion with the model described by the P-wave velocities V_{Pz}, V_{Px}, and V_{Py} in the coordinate directions and the NMO velocities V_{nmo1}, V_{nmo2}, and V_{nmo3}.

A synthetic example for a complicated geologic structure shows that WI can reconstruct high-resolution fields of the velocities V_{Pz}, V_{Px}, and V_{Py} from wide-azimuth surface P-wave data. However, synthetic examples also reveal significant trade-offs among the model parameters, which reduce the accuracy of the inverted NMO velocities V_{nmo1}, V_{nmo2}, and V_{nmo3}. Although the low-wavelength fields of the NMO velocities are constrained by reflection traveltimes, their higher-frequency components are not well resolved by WI. Overall, this work demonstrates the feasibility of waveform inversion of wide-azimuth surface data for acoustic orthorhombic media.

ACKNOWLEDGMENTS

REFERENCES

Albertin, U., Shen, P., Sekar, A., Johnsen, T., Wu, C., Nihei, K. and Bube, K., 2016. 3D orthorhombic elastic full-waveform inversion in the reflection domain from hydrophone data. Expanded Abstr., 86th Ann. Internat. SEG Mtg., Dallas: 1094-1098.

Alkhalifah, T., 1998. Acoustic approximations for processing in transversely isotropic media. Geophysics, 63: 623-631.

Alkhalifah, T., 2000. An acoustic wave equation for anisotropic media. Geophysics, 65: 1239-1250.

Alkhalifah, T., Masmoudi, N. and Oh, J.-W., 2016. A recipe for practical full-waveform inversion in orthorhombic anisotropy. Expanded Abstr., 86th Ann. Internat. SEG Mtg., Dallas: 317-321.

Aminzadeh, F., Brac, J. and Kunz, T., 1997. 3D salt and overthrust model. Modeling Series I, SEG, Tulsa, OK.

Baydin, V., Charara, M. and Dovgilovich, L., 2015. Elastic orthorhombic full-waveform inversion for 3D VSP case. Extended Abstr., 77th EAGE Conf., Madrid: 1-5.

Benson, S.J. and Moré, J.J., 2001. A limited memory variable metric method in subspaces and bound constrained optimization problems. Technical Report, ANL/ACS-P909-0901, Argonne National Labor.

Birdus, S., Sun, J., Sun, W., Xie, Y., Gazzoli, M., Andreolli, M. and Ursulic, A., 2012. Multi-azimuth PSDM processing in the presence of orthorhombic anisotropy − a case history offshore north west Australia. Expanded Abstr., 82nd Ann. Internat. SEG Mtg., Las Vegas: 1-5.

Chen, P., 2011. Full-wave seismic data assimilation: theoretical background and recent advances. Pure Appl. Geophys., 168: 1527-1552.

Du, X., Fowler, P.J. and Fletcher, R.P., 2014. Recursive integral time-extrapolation methods for waves: A comparative review. Geophysics, 79(1): T9-T26.

Duveneck, E. and Bakker, P.M., 2011. Stable P-wave modeling for reverse-time migration in tilted TI media. Geophysics, 76(2): S65–S75.

Etgen, J.T. and Dellinger, J., 1989. Accurate wave equation modeling. Expanded Abstr., 59th Ann. Internat. SEG Mtg., Dallas: 494–497.

Fichtner, A., 2010. Full Seismic Waveform Modelling and Inversion. Springer Verlag, Berlin.

Fichtner, A., Bunge, H.-P. and Igel, H., 2006a. The adjoint method in seismology: I. Theory. hys. Earth Planet. Inter., 157: 86-104.

Fichtner, A., Bunge, H.-P. and Igel, H., 2006b. The adjoint method in seismology: II. Applications: traveltimes and sensitivity functionals. Phys. Earth Planet. Inter., 157: 105-123.

Fletcher, R.P., Du, X. and Fowler, P., 2008. A new pseudo-acoustic wave equation for TI media. Expanded Abstr.,78th Ann. Internat. SEG Mtg., Las Vegas: 2082-2086.

Fletcher, R.P., Du, X. and Fowler, P.J., 2009. Reverse time migration in tilted transversely isotropic (TTI) media. Geophysics, 74(6): WCA179-WCA187.

Fomel, S., Sava, P., Vlad, I., Liu, Y. and Bashkardin, V., 2013a. Madagascar: Open-source software project for multidimensional data analysis and reproducible computational experiments. J. Open Res. Softw., 1: e8.

Fomel, S., Ying, L. and Song, X., 2013b. Seismic wave extrapolation using lowrank symbol approximation: Geophys. Prosp., 61: 526-536.

Fowler, P., 2015. Some pitfalls in orthorhombic parameter estimation. Expanded Abstr., 85th Ann. Internat. SEG Mtg., New Orleans: 493-497.

Fowler, P.J., Du, X. and Fletcher, R.P., 2010. Coupled equations for reverse time migration in transversely isotropic media. Geophysics, 75(1): S11-S22.

Fowler, P.J. and King, R., 2011. Modeling and reverse time migration of orthorhombic pseudoacoustic P-waves Expanded Abstr., 81st Ann. Internat. SEG Mtg., San Antonio: 190-195.

Fowler, P.J. and Lapilli, C., 2012. Generalized pseudospectral methods for orthorhombic modeling and reverse-time migration. Expanded Abstr., 82nd Ann. Internat. SEG Mtg., Las Vegas: 1-5.

222

Gholami, Y., Brossier, R., Operto, S., Prieux, V., Ribodetti, A. and Virieux, J., 2013. Which parameterization is suitable for acoustic vertical transverse isotropic full waveform inversion? Part 2: Synthetic and real data case studies from Valhall. Geophysics, 78(2): R107-R124.

Grechka, V., Zhang, L. and Rector, J.W., 2004. Shear waves in acoustic anisotropic media. Geophysics, 69: 576-582.

Kamath, N. and Tsvankin, I., 2013. Full-waveform inversion of multicomponent data for horizontally layered VTI media. Geophysics, 78(5): WC113-WC121.

Kamath, N. and Tsvankin, I., 2016. Elastic full-waveform inversion for VTI media: Methodology and sensitivity analysis. Geophysics, 81(2): C53-C68.

Karazincir, M. and Orumwense, R., 2014. Tilted orthorhombic velocity model building and imaging of Zamzama gas field with full-azimuth land data. The Leading Edge, 33: 1024-1028.

Kolda, T.G., O'Leary, D.P. and Nazareth, L., 1998. BFGS with update skipping and varying memory. SIAM J. Optimizat., 8: 1060-1083.

Kosloff, D.D. and Baysal, E., 1982. Forward modeling by a Fourier method. Geophysics, 47: 1402-1412.

Lailly, P., 1983. The seismic inverse problem as a sequence of before stack migrations. Conf. Inver. Scatter.: Theory Applicat., Soc. Industr. Appl. Mathemat., Philadelphia, PA: 206-220.

Liu, D.C. and Nocedal, J., 1989. On the limited memory BFGS method for large scale optimization. Mathemat. Programm., 45: 503-528.

Liu, Q. and Tromp, J. 2008. Finite-frequency sensitivity kernels for global seismic wave propagation based upon adjoint methods. Geophys. J. Internat., 174: 265-286.

Luo, J. and Wu, R.-S., 2015. Seismic envelope inversion: reduction of local minima and noise resistance. Geophys. Prosp., 63: 597-614.

Masmoudi, N. and Alkhalifah, T., 2016. A new parametrization for waveform inversion in acoustic orthorhombic media. Geophysics, 81(4): R157-R171.

Mathewson, J., Bachrach, R., Ortin, M., Decker, M., Kainkaryam, S., Cegna, A., Paramo, P., Vincent, K. and Kommedal, J., 2015. Offshore Trinidad tilted orthorhombic imaging of full-azimuth OBC data. Expanded Abstr., 85th Ann. Internat. SEG Mtg., New Orleans: 356-360.

Nocedal, J., 1992. Theory of algorithms for unconstrained optimization. Acta Numer., 1: 199-242.

Nocedal, J. and Wright, S., 2006. Numerical Optimization. Springer Science & Business Media.

Oh, J.-W. and Alkhalifah, T., 2016. 3D elastic-orthorhombic anisotropic full-waveform inversion. Application to field OBC data. Expanded Abstr., 86th Ann. Internat. SEG Mtg., Dallas: 1206-1210.

Pestana, R.C. and Stoffa, P.L., 2010. Time evolution of the wave equation using rapid expansion method: Geophysics, 75(4): T121-T131.

Plessix, R.-E., 2006. A review of the adjoint-state method for computing the gradient of a functional with geophysical applications. Geophys. J. Internat., 167: 495-503.

Royle, G., 2011. Viscoelastic orthorhombic full wavefield inversion: Development of multiparameter inversion methods. Expanded Abstr., 81st Ann. Internat. SEG Mtg., San Antonio: 4329-4333.

Song, X. and Alkhalifah, T., 2013. Modeling of pseudo-acoustic P-waves in orthorhombic media with low-rank approximation. Geophysics, 78(4): C33-C40.

Tal-Ezer, H., 1986. Spectral methods in time for hyperbolic equations. SIAM J. Numer. Analys., 23: 11-26.

Tal-Ezer, H., Kosloff, D. and Koren, Z., 1987. An accurate scheme for seismic forward modeling. Geophys. Prosp., 35: 479-490.

Tarantola, A., 1984. Inversion of seismic reflection data in the acoustic approximation. Geophysics, 49: 1259-1266.

Tarantola, A., 1988. Theoretical background for the inversion of seismic waveforms including elasticity and attenuation. Pure Appl. Geophys., 128: 365-399.

Thiébaut, E., 2002. Optimization issues in blind deconvolution algorithms. Astronomical Telescopes and Instrumentation, Internat. Soc. Optics Photonics, 174183.

Thomas, M., Mothi, S. and McGill, P., 2012. Improving subsalt images using tilted-orthorhombic RTM in Green Canyon, Gulf of Mexico. Expanded Abstr., 82nd Ann. Internat. SEG Mtg., Las Vegas: 1-5.

Tromp, J., Tape, C. and Liu, Q., 2005. Seismic tomography, adjoint methods, time reversal and banana-doughnut kernels. Geophys. J. Internat., 160: 195-216.

Tsvankin, I., 1997. Anisotropic parameters and P-wave velocity for orthorhombic media. Geophysics, 62: 1292-1309.

Tsvankin, I., 2012. Seismic Signatures and Analysis of Reflection Data in Anisotropic Media. SEG, Tulsa, OK.

Tsvankin, I. and Grechka, V., 2011. Seismology of Azimuthally Anisotropic Media and Seismic Fracture Characterization. SEG, Tulsa, OK.

Wang, S. and Wilkinson, D., 2012. Imaging for unconventional resource plays using an orthorhombic velocity model. Expanded Abstr., 82nd Ann. Internat. SEG Mtg., Las Vegas:, 1-5.

Wu, R.-S., Luo, J. and Wu, B., 2014. Seismic envelope inversion and modulation signal model. Geophysics, 79(3): WA13-WA24.

Xie, Y., Zhou, B., Zhou, J., Hu, J., Xu, L., Wu, X., Lin, N., Loh, F.C., Liu, L. and Wang, Z., 2017. Orthorhombic full-waveform inversion for imaging the Luda field using wide-azimuth ocean-bottom-cable data. The Leading Edge, 36: 75-80.

Zhang, H.J. and Zhang, Y., 2011. Reverse time migration in vertical and tilted orthorhombic media. Expanded Abstr., 81st Ann. Internat. SEG Mtg., San Antonio: 185-189.

Zhang, Y. and Zhang, G., 2009. One-step extrapolation method for reverse time migration. Geophysics, 74(4): A29-A33.

Zhou, H., Zhang, G. and Bloor, R., 2006a. An anisotropic acoustic wave equation for modeling and migration in 2D TTI media. Expanded Abstr., 76th Ann. Internat. SEG Mtg., New Orleans: 194–198.

Zhou, H., Zhang, G. and Bloor, R., 2006b. An anisotropic acoustic wave equation for VTI media. Extended Abstr., 68th EAGE Conf., Vienna: 1-5.

APPENDIX

P-WAVE DISPERSION RELATION IN ACOUSTIC ORTHORHOMBIC MEDIA

As discussed by (Tsvankin, 1997, 2012), P-wave kinematic signatures in orthorhombic media are fully controlled by the vertical velocity V_{P0} and five anisotropy parameters (the coordinate planes are assumed to coincide with the planes of symmetry):

$$V_{P0} = \sqrt{\frac{c_{33}}{\rho}} \quad - \quad \text{the P-wave vertical velocity,}$$

$$(A-1)$$

$$\varepsilon^{(1)} = \frac{c_{22} - c_{33}}{2c_{33}} \quad - \quad \text{the VTI parameter } \varepsilon \text{ in the } [x_2, x_3]\text{--plane,} \tag{A-2}$$

$$\varepsilon^{(2)} = \frac{c_{11} - c_{33}}{2c_{33}} \quad - \quad \text{the VTI parameter } \varepsilon \text{ in the } [x_1, x_3]\text{--plane,} \tag{A-3}$$

$$\delta^{(1)} = \frac{(c_{23} + c_{44})^2 - (c_{33} - c_{44})^2}{2c_{33}(c_{33} - c_{44})} \quad - \quad \text{the VTI parameter } \delta \text{ in the } [x_2, x_3]\text{--plane,} \tag{A-4}$$

$$\delta^{(2)} = \frac{(c_{13} + c_{55})^2 - (c_{33} - c_{55})^2}{2c_{33}(c_{33} - c_{55})} \quad - \quad \text{the VTI parameter } \delta \text{ in the } [x_1, x_3]\text{--plane,} \tag{A-5}$$

$$\delta^{(3)} = \frac{(c_{12} + c_{66})^2 - (c_{11} - c_{66})^2}{2c_{11}(c_{11} - c_{66})} \quad - \quad \text{the VTI parameter } \delta \text{ in the } [x_1, x_2]\text{--plane.} \tag{A-6}$$

The superscripts refer to the axis orthogonal to the corresponding plane. Then the Christoffel matrix [eq. (3)] can be written as

$$\mathbf{G} = \begin{bmatrix} k_x^2 \, V_{\mathrm{P0}}^2(1 + 2\varepsilon^{(2)}) & k_x k_y V_{\mathrm{P0}}^2(1 + 2\varepsilon^{(2)})\sqrt{1 + 2\delta^{(3)}} & k_x k_z V_{\mathrm{P0}}^2\sqrt{1 + 2\delta^{(2)}} \\ k_x k_y V_{\mathrm{P0}}^2(1 + 2\varepsilon^{(2)})\sqrt{1 + 2\delta^{(3)}} & k_y^2 \, V_{\mathrm{P0}}^2(1 + 2\varepsilon^{(1)}) & k_y k_z V_{\mathrm{P0}}^2\sqrt{1 + 2\delta^{(1)}} \\ k_x k_z V_{\mathrm{P0}}^2\sqrt{1 + 2\delta^{(2)}} & k_y k_z V_{\mathrm{P0}}^2\sqrt{1 + 2\delta^{(1)}} & k_z^2 \, V_{\mathrm{P0}}^2 \end{bmatrix}. \tag{A-7}$$

Symbolically we represent eq. (A-7) as

$$\mathbf{G} = \mathbf{K}\mathbf{M}\mathbf{K}^{\mathsf{T}}, \tag{A-8}$$

where

$$\mathbf{K} = \begin{bmatrix} k_x & & \\ & k_y & \\ & & k_z \end{bmatrix},$$

(A-9)

and

$$\mathbf{M} = \begin{bmatrix} V_{\mathrm{P0}}^2(1+2\varepsilon^{(2)}) & V_{\mathrm{P0}}^2(1+2\varepsilon^{(2)})\sqrt{1+2\delta^{(3)}} & V_{\mathrm{P0}}^2\sqrt{1+2\delta^{(2)}} \\ V_{\mathrm{P0}}^2(1+2\varepsilon^{(2)})\sqrt{1+2\delta^{(3)}} & V_{\mathrm{P0}}^2(1+2\varepsilon^{(1)}) & V_{\mathrm{P0}}^2\sqrt{1+2\delta^{(1)}} \\ V_{\mathrm{P0}}^2\sqrt{1+2\delta^{(2)}} & V_{\mathrm{P0}}^2\sqrt{1+2\delta^{(1)}} & V_{\mathrm{P0}}^2 \end{bmatrix}.$$

(A-10)

Substituting the matrix $\mathbf{G}$ into the characteristic eq. (4) yields a cubic equation for ω^2:

$$\omega^6 + a_0\,\omega^4 + a_1\,\omega^2 + a_2 = 0,$$

(A-11)

where

$$a_0 = -\left[(1+\epsilon^{(2)})k_x^2 + (1+\epsilon^{(1)})k_y^2 + k_z^2\right]V_{\mathrm{P0}}^2,$$

(A-12)

$$a_1 = \left\{(1+2\epsilon^{(2)})\left[(1+2\epsilon^{(1)}) - (1+2\epsilon^{(2)})(1+2\delta^{(3)})\right]k_x^2 k_y^2 \right. \\ \left. + 2(\epsilon^{(2)} - \delta^{(2)})k_x^2 k_z^2 + 2(\epsilon^{(1)} - \delta^{(1)})k_y^2 k_z^2\right\}V_{\mathrm{P0}}^4,$$

(A-13)

$$a_2 = \left[(1+2\epsilon^{(2)})^2(1+2\delta^{(3)}) - (1+2\epsilon^{(2)})(2\epsilon^{(1)} - 2\delta^{(1)}) + (1+2\delta^{(2)})(1+2\epsilon^{(1)}) \right. \\ \left. - 2(1+2\epsilon^{(2)})\sqrt{1+2\delta^{(2)}}\sqrt{1+2\delta^{(1)}}\sqrt{1+2\delta^{(3)}}\right]k_x^2 k_y^2 k_z^2\, V_{\mathrm{P0}}^6.$$

(A-14)

Our waveform-inversion algorithm operates with the P-wave velocities V_{Px}, V_{Py}, and V_{Pz} in the coordinate directions, and the NMO velocities $V_{nmo}^{(1)}$, $V_{nmo}^{(2)}$, and $V^{(3)}$:

$$V_{Pz} = V_{P0} , \tag{A-15}$$

$$V_{Px} = V_{P0}\sqrt{1 + 2\varepsilon^{(2)}} , \tag{A-16}$$

$$V_{Py} = V_{P0}\sqrt{1 + 2\varepsilon^{(1)}} , \tag{A-17}$$

$$V_{nmo}^{(1)} = V_{P0}\sqrt{1 + 2\delta^{(1)}} , \tag{A-18}$$

$$V_{nmo}^{(2)} = V_{P0}\sqrt{1 + 2\delta^{(2)}} , \tag{A-19}$$

$$V_{nmo}^{(3)} = V_{Px}\sqrt{1 + 2\delta^{(3)}} . \tag{A-20}$$

The coefficients a_0, a_1, and a_2 in eqs. (A-12) - (A-14) then take the form:

$$a_0 = -\left[V_{Px}^2 k_x^2 + V_{Py}^2 k_y^2 + V_{Pz}^2 k_z^2 \right] , \tag{A-21}$$

$$a_1 = V_{Pz}^2[V_{Px}^2 - (V_{nmo}^{(2)})^2]k_x^2 k_z^2 + V_{Pz}^2[V_{Py}^2 - (V_{nmo}^{(1)})^2]k_y^2 k_z^2 + V_{Px}^2[V_{Py}^2 - (V_{nmo}^{(3)})^2]k_x^2 k_y^2 , \tag{A-22}$$

$$a_2 = \left\{ V_{Pz}^2 V_{Px}^2 \left[(V_{nmo}^{(3)})^2 + (V_{nmo}^{(1)})^2 \right] - 2V_{Pz}^2 V_{Px} V_{nmo}^{(1)} V_{nmo}^{(2)} V_{nmo}^{(3)} \right.$$
$$\left. + V_{Pz}^2 V_{Py}^2 (V_{nmo}^{(2)})^2 - V_{Pz}^2 V_{Px}^2 V_{Py}^2 \right\} k_x^2 k_y^2 k_z^2 . \tag{A-23}$$

The P-wave dispersion relation is obtained analytically by solving the cubic eq. (A-11).